



Characteristics of fractures stimulated by supercritical carbon dioxide fracturing in shale based on acoustic emission monitoring

Shan Wu^{a,b}, Hongkui Ge^{b,*}, Tiantai Li^c, Xiaoqiong Wang^b, Ning Li^b, Yushi Zou^b, Ke Gao^{a,**}

^a Department of Earth and Space Sciences, Southern University of Science and Technology, Shenzhen, 518055, Guangdong, China

^b China University of Petroleum (Beijing), Beijing, 102249, China

^c Xi'an Shiyou University, Xi'an, 710065, Shanxi, China

ABSTRACT

In recent years, supercritical carbon dioxide (SC-CO₂) has been attempted in hydraulic fracturing in shale reservoirs as a new type of fracturing tool to overcome the drawback of traditional water-based fluids. Because of the unique physical and chemical properties of SC-CO₂, its fracturing mechanism is more complicated than traditional fluids and still unclear at present. In this paper, we hydraulically fracture a shale reservoir rock using SC-CO₂ and monitor the fracturing process using acoustic emission (AE) data. The results show the fractures stimulated by SC-CO₂ composite of both shear and tensile fractures. In the initiation stage, SC-CO₂ activates the natural fractures around the wellbore and induces shear fractures. In the propagation stage, SC-CO₂ permeates the fracture tips quickly, results in a dynamic propagation process, and generates plenty of tensile fractures. The phase change of CO₂ could be observed during the fracture propagation process, which is accompanied by a rapid pressure change and local stress shock formations in the fractures. Additionally, the experiments also demonstrate that the existence of bedding structures in shale could constrain the propagation of fractures, thus leading to a smaller volume of fracture network and limiting the complexity of the generated fractures. This research may help understand the fracturing mechanism of SC-CO₂ and shed light on the development of hydraulic fracturing technology in shale reservoirs.

1. Introduction

High-pressure water is injected into reservoirs to stimulate complex fracture networks consisting of hydraulic fractures and natural fractures.¹ This complex fracture network increases the stimulated reservoir volume and plays an important role in enhancing shale gas production.^{2,3} Currently, water-based hydraulic fluids are commonly used; however, water-based fracturing fluids may result in fluid retention effects.^{4,5} And also, water shortage is another critical difficulty for fracturing operations for places. To eliminate the problems caused by water-based fracturing fluids, the exploration of non-water fracturing fluids is becoming necessary. Among the many non-water fracturing fluids, supercritical carbon dioxide (SC-CO₂) seems to be one of the best alternatives to water-based fracturing fluids because of its special physical and chemical properties. For example, it has zero water sensitivity and could thus avoid clay swelling; it is also of low viscosity and high diffusion capacity, making it an efficient tool to transmit energy to reservoir rocks.⁶

Scattered researches have been found to explore the capability of SC-CO₂ as a new fracturing fluid.⁷ However, there is still no consensus about

whether SC-CO₂ can promote the fracturing effect. According to the generated fracture pattern from laboratory experiments, Zhou et al.⁸ found that the SC-CO₂ fracturing is a mechanical-chemical-thermal coupling process. Such a multi-field coupling process may induce more complex fracture networks than that induced by water-based fracturing fluid.^{8,9} Another view is that SC-CO₂ has a very low viscosity, making it easy to be filtered out along bedding structures in shale reservoirs,^{10–12} and consequently, the leakage of SC-CO₂ may limit the fracturing area. There are also concerns that the width of fractures formed by SC-CO₂ is generally small, and it is thus not conducive to the migration of proppants, which could also decrease the effect of SC-CO₂ fracturing.^{13,14} To date, it is still not clear whether SC-CO₂ is effective and efficient for shale fracturing.

Since the fracturing process of SC-CO₂ is generally coupled with chemical processes, it is difficult to investigate its fracturing mechanism and fracture characteristics using pure numerical methods. Therefore, laboratory experiments with fracturing monitoring techniques have to be employed. True triaxial hydraulic fracturing experiments are commonly used to realize real fracturing conditions, together with the usage of acoustic emission (AE) for monitoring the whole dynamic

* Corresponding author.

** Corresponding author.

E-mail addresses: gehongkui@163.com (H. Ge), gaok@sustech.edu.cn (K. Gao).

<https://doi.org/10.1016/j.ijmms.2022.105065>

Received 3 August 2021; Received in revised form 17 January 2022; Accepted 15 February 2022

Available online 21 February 2022

1365-1609/© 2022 Elsevier Ltd. All rights reserved.

fracturing process.^{15–17} The AE results provide a critical basis for estimating the fracture morphology, propagation trends, and understanding the fracture mechanisms.¹⁸ However, shales usually have apparent anisotropy, making it challenging to accurately pinpoint AE events and the fracture mechanism. Previous research of SC-CO₂ fracturing was mainly completed in isotropic rocks such as granite.¹⁹ For shale, Li et al.²⁰ located AE events using algorithms with an anisotropic velocity model and proposed that the layered model is more suitable for AE event location in shales. But there is no further research about the SC-CO₂ fracturing in shale based on the AE location from the algorithms with an anisotropic velocity model. Zhang et al.²¹ and Zou et al.²² used the AE rates as an assistant to computed tomography (CT) images and proved that the SC-CO₂ could enhance the complexity of the generated fracture network. Without the AE location results, there is no definite explanation for the critical phenomena in the experiments of SC-CO₂ fracturing. For example, it has been observed that the initiation pressure is lower than the theoretical value²¹; however, there is no evidence to prove whether it is caused by the reduction of effective stress in the fractures or the activation of natural fractures. This problem can be studied by investigating the AE event location results and the mechanical properties of fractures.

Another problem in the SC-CO₂ fracturing process is the phase change. Zhou & Zhang²³ explained the possibility of phase change in theory. However, phase change has not been observed in their experiment. The process of phase change directly affects the source of AE. In the laboratory scale rupture, there may be overlaps of various sources in the time domain. At the same time, it is hard to distinguish such differences of the source with the inversion results. Therefore, it is necessary to use the frequency information of AE waveforms to reflect the characteristics of the source. At present, research on the frequency of AE waveforms to reveal the mechanism of phase change is still lacking. More experimental studies of the SC-CO₂ fracturing by AE monitoring should be conducted.

This paper studies the fracture characteristics of SC-CO₂ fracturing based on AE monitoring. AE event location, source mechanism, and waveform frequency are calculated. Based on the AE results and the comparison with water fracturing, the fracture morphology and fracture

mechanism characteristics under SC-CO₂ fracturing are obtained. The paper is organized as follows. The samples, equipment, and procedures of the experiments are briefly introduced in Section 2. In Section 3, we overview the methods used to analyze AE data and present the results obtained from the analysis. In Section 4, we compare the experimental results of SC-CO₂ fracturing with those of water fracturing. This is followed by a discussion of the particularity of SC-CO₂ fracturing. The conclusion is given at the end.

2. Experimental samples, equipment, and procedures

The rock sample used in the current experiment is shale from an outcrop of Longmaxi (LMX) formation in China (Fig. 1a). The Young's modulus and Poisson's ratio of the sample are near 40 GPa and 0.2, respectively. There are many bedding structures in the sample where specific openings or weak cementation can be found. Each rock sample is cut into a 300 × 300 × 300 mm³ cube with all ends well polished. A hole with a diameter of 1.6 cm is drilled parallel to σ_h to simulate the wellbore. The length of the wellbore is 13.5 cm, and the end without steel pipe is kept at 3 cm (Fig. 1b).

The experimental system has two main parts. The first part is the true triaxial fracturing simulation equipment developed at the China University of Petroleum (Beijing), which can apply boundary forces from three orthogonal directions to simulate the stress condition underground (Fig. 1c). The boundary loading acting in the vertical direction (i.e., perpendicular to the bedding plane) on the sample is denoted as σ_v , and the other two horizontal boundary loadings are respectively denoted as σ_H and σ_h , as shown in Fig. 1c. CO₂ becomes supercritical when the temperature exceeds 31.3 °C and pressure is over 7.38 MPa. To ensure that CO₂ becomes supercritical and is injected at a constant rate, CO₂ is released to a cooling unit for liquefying until it transfers to the liquid state. Then, we pump liquid CO₂ into a fluid separation vessel for increasing fluid pressure to 6.3 MPa. After that, we inject the liquid CO₂ into the heating-pressuring pipelines to reach the supercritical state at a constant rate. The heating-pressure pipelines warm up to 80 °C according to the formation temperature. Moreover, the sample is heated to 80 °C by heating panels attached to the loading plates from one day

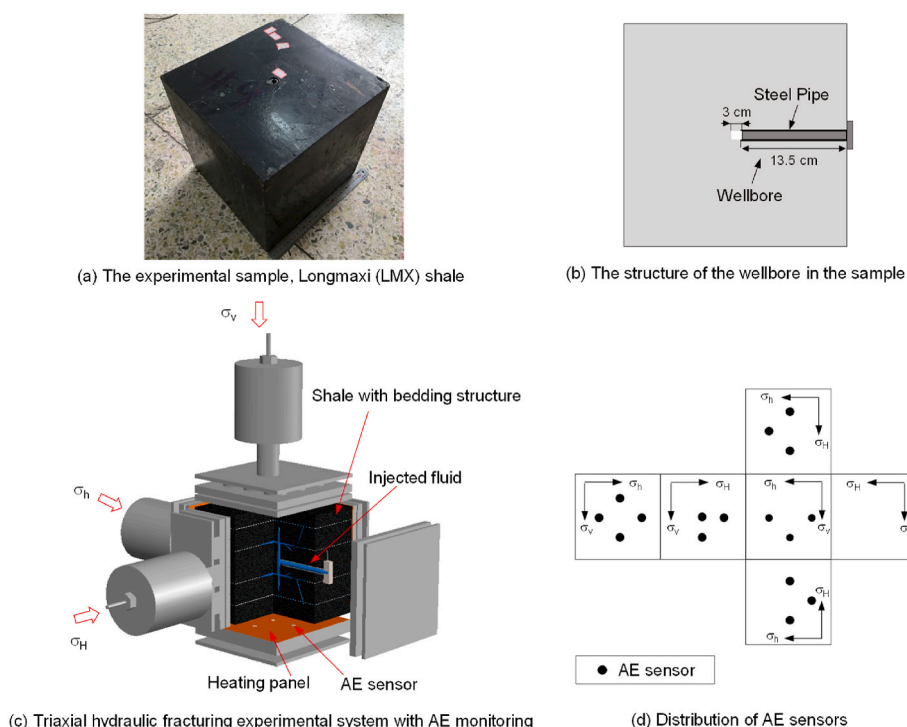


Fig. 1. Schematic diagram of the sample and experimental system.

before the experiment until the ending of the experiment, thus ensuring that the internal temperature of the sample holds at 80 °C. This injection procedure can guarantee successful SC-CO₂ fracturing in shale and sandstone.^{9,22}

The other part is the AE monitoring system. The multi-channel continuous waveform monitoring equipment named DS5 from Beijing Softland Company is used for acquiring the AE waveform. The AE sensor is the type of RS-2A from the same company, and it has a stable frequency response at 50–400 kHz. Sixteen sensors are arranged on the five surfaces (i.e., top, left, right, front, and back) of the sample (Fig. 1 d). The sensor coverage to the sample satisfies the far-field source assumption for AE analysis. The amplitude threshold of each sensor is set to 100 mV, and the preamplifier is 40 dB; continuous waveform acquisition mode is adopted, and the sampling rate is set to 3 MHz per sensor. The pencil lead-breaking calibration in terms of amplitude has been conducted, which provides data for verifying AE event location and moment tensor inversion. We also calibrated the sensor and algorithm following Ono²⁴ and Grosse & Ohtsu.²⁵ A more detailed introduction of the testing system is given by Zou et al.,²⁶ and a complete illustration of the experimental setup can be found in Wu et al.²⁷

Conducting hydraulic fracturing experiments successfully in shale is usually challenging because it could be influenced by many factors. We discuss the SC-CO₂ fracturing by comparing it with a series of water fracturing experiments reported earlier using the same type of rock samples and equipment.^{20,28} Due to the existence of bedding structures, it is easy to cause failure in such experiments. This has also been proved in previous fracturing experiments in LMX shale. We have successfully achieved a complete set of SC-CO₂ fracturing results and obtained the complete acoustic emission information (Fig. 2a). The boundary loading used in this experiment is $\sigma_h = 10$ MPa, $\sigma_H = 15$ MPa, and $\sigma_v = 20$ MPa, which is similar to the in situ stress in the field where $\sigma_v \geq \sigma_H > \sigma_h$ and is corresponding to the stress in the experiment of water fracturing.²⁰ The

injection rate of SC-CO₂ is maintained constant at 5 ml/min.

3. Experimental results

3.1. Evolution of injection pressure and AE events

AE waveforms are commonly used to demonstrate AE behavior during the injection process from an overall perspective of SC-CO₂ fracturing, which reflects the performance of AE rates and amplitude of AE events that can indicate the characteristic of AE in SC-CO₂ fracturing.^{29,30} The injection pressure curve of SC-CO₂ and the waveform of generated AE are presented in Fig. 2a. The pressure curve shows a weak fluctuation. The initiation pressure of SC-CO₂ fracturing is 9.6 MPa, which is much lower than the theoretical value in the fracturing theory for water-based fluid.²¹ Generally, the fracturing stage before the initiation pressure is called the initiation stage, followed by the fracture propagation stage. The injection pressure in the fracture propagation stage is below the minimum boundary loading as shown in Figs. 2a and 3a. Similar phenomena have also been reported in other experiments of SC-CO₂ fracturing.^{19,21,22} This may be attributed to the volume expansion of CO₂ once hydraulic fractures formed and even penetrated the sample. From the AE waveform sequence, many AE events can be observed. In the initiation stage, the amplitude of the AE waveform is small, making the AE waveform barely observable in the whole sequence of the waveform. There are many AE waveforms with large amplitudes in the propagation stage. We have picked 235 AE events for source location and moment tensor analysis.

The statistical parameters of AE events obtained from the sequence of AE waveform can directly reflect the dynamic characteristics of the fracturing process. The most frequently used statistical parameters are the AE rate and *b*-value.^{31,32} The AE rate is the number of AE events per unit time. The change of AE rate is usually used to interpret fracture

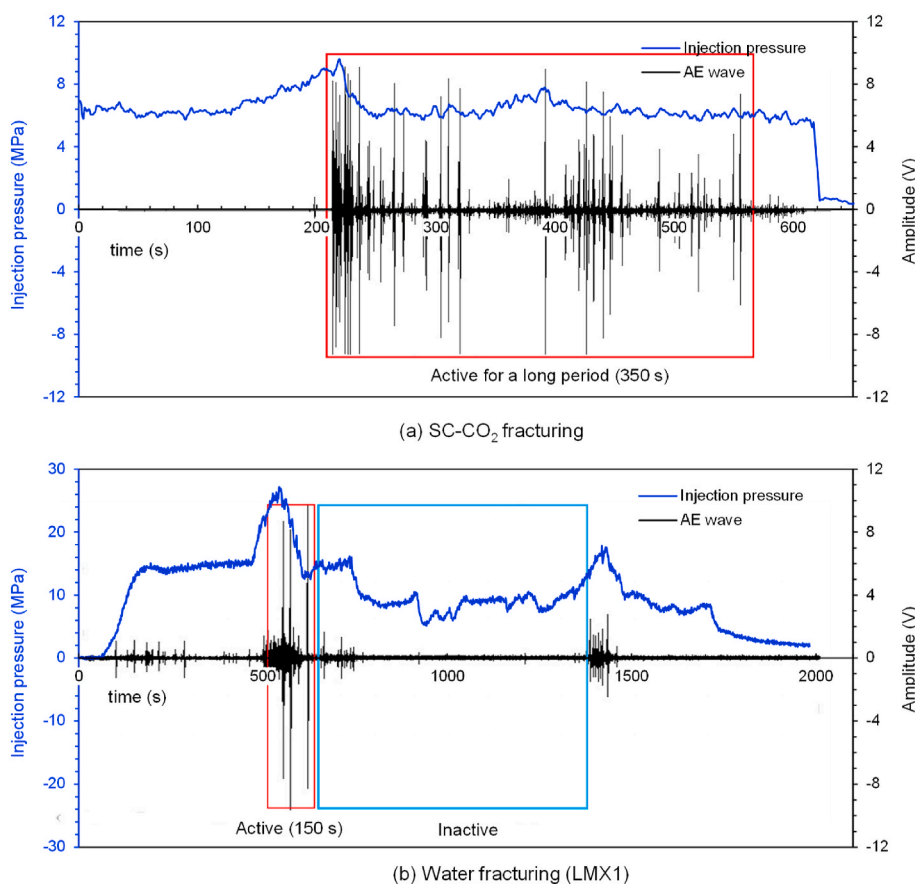


Fig. 2. Injection pressure curve and AE waveform of (a) SC-CO₂ fracturing and (b) water fracturing experiments. The SC-CO₂ fracturing experiment shows a long period (350 s) containing high amplitude AE waveforms, which lasts almost from the initiation to the end of the whole fracturing process. In the water fracturing experiment, the active time with a high amplitude AE waveform lasts only about 150 s, followed by a long “quiet” time. The waveform shown here is recorded by an AE sensor located on the bottom surface of the sample, which has a high ratio of signal to noise.

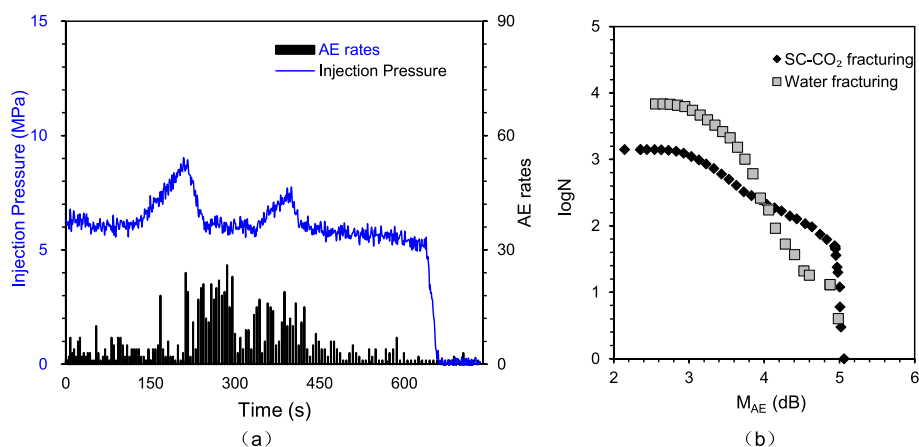


Fig. 3. (a) AE rates and injection pressure of SC-CO₂ fracturing. The AE rate fluctuates with the change of injection pressure. After the first injection pressure peak point, the AE rate keeps a high value until after the second injection pressure peak point. (b) The distribution of AE amplitude for both SC-CO₂ fracturing and water fracturing.

convergence and nucleation in rock mechanics experiments. The unstable propagation of cracks generally corresponds to a rapid increase in AE rate. The increase of AE rate further signifies the sudden change of stress inside the rock. As an important parameter related to fracture activity, the sudden increase of AE rate can be used as a macroscopic fracture formation indicator. Fig. 3a shows the AE rates over time; the evolution of the injection pressure is also plotted for comparison. The AE rate remains high for a while and reaches its first peak value at nearly 210 s. Afterward, we can observe a gradual decrease in AE rate. This is different from the fracturing experiments with water-based fluid in which a sharp drop of the number of AE events could be observed after the peak value (Fig. 2b). We will discuss this in detail in a later section.

The statistics of the amplitude of AE events obey the Gutenberg-Richter formula.³³ The b -value is the slope of the amplitude distribution curve, which directly reflects the character of energy distribution in the failure process.³⁴ When more AE events with large amplitude are generated, a smaller b -value will be yielded, and vice versa. The amplitude of AE waveform is positively correlated with the fracture size, i.e., a lower b -value indicates that macroscopic cracks are easy to form. In our analysis, the b -value of AE can be calculated using

$$\log_{10} N = a - b \times \frac{A_{dB}}{20} \quad (1)$$

where A_{dB} is the amplitude of AE waveform expressed in the unit of dB, i.e.,

$$A_{dB} = 10 \log_{10} A_{\max}^2 = 20 \log_{10} A_{\max} \quad (2)$$

and A_{\max} is the amplitude of AE expressed in the unit of μV .³³

The distribution of AE amplitude of SC-CO₂ fracturing is also different from that of water fracturing, as shown in Fig. 3b. The results of water fracturing are from the same experimental system conducted earlier, and the details of which can be found in Wu et al.²⁷ There are more AE events with amplitude higher than 4 in the SC-CO₂ fracturing, and thus a smaller b -value (smaller slope) is generated.

3.2. AE event location and fractal analysis of generated fractures

The locations of AE events reflect the positions of the generated fractures. We use the location of AE events to monitor the dynamic fracture propagation process. The AE event located inside the rock can be interpreted based on the arrival time of the P -wave.³⁵ The calculation of AE event location adopts the combination of the classical Geige method and double-difference method.^{36,37} Since shale is composed of layered depositions, we use the transversely isotropic model to describe the P -wave anisotropy, which will reduce the location error. For the

location and the moment tensor inversion later, we select the AE events, which are monitored by at least 11 AE sensors. The arrival times and the amplitudes were determined from the AE waveform by the STA/LTA-AIC picker method.^{38,39} In the whole process of the experiment, we have obtained 235 AE events after selection. Fig. 4 displays the spatial locations of all the AE events by dot, and Fig. 5 shows their projections on the three surfaces according to the axes. The AE event locations are scattered, and there are only a few dots near the injection point. Many fractures spread to the boundary. This fracture morphology is far from the planar fractures and shows the characteristics of complex fracture networks.

Hydraulic fractures are usually assumed to be planar.^{40,41} The planar fracture can be characterized by its length, height, and width.⁴² However, the AE event location of SC-CO₂ fracturing indicates that the fractures are distributed more dispersed in space, which is quite different from the planar fracture.²³ For complicated fracture networks, it is common to characterize them quantitatively using the fractal method. Lei⁴³ used the correlation dimension to describe the nucleation process of fractures during the uniaxial compression tests of rocks. Li

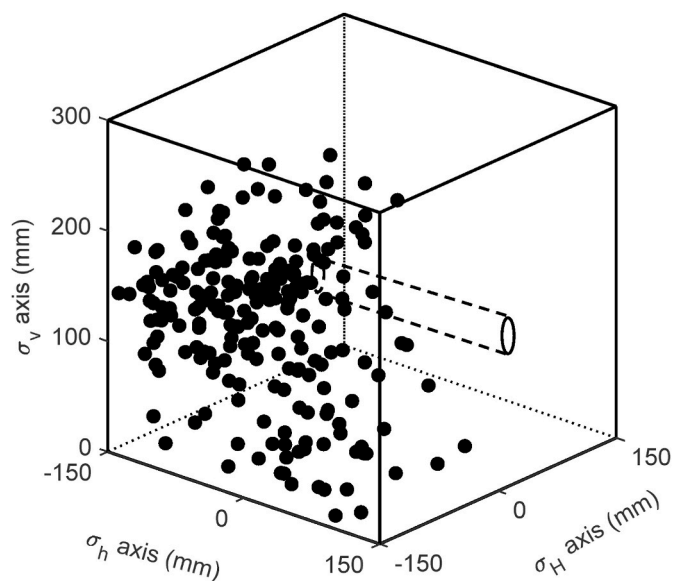


Fig. 4. The locations of AE events of SC-CO₂ fracturing. It shows all the 235 AE events in the experiment. The AE event location of SC-CO₂ fracturing is more dispersed in space compared with the result of water fracturing (will be discussed in detail in the Discussion section).

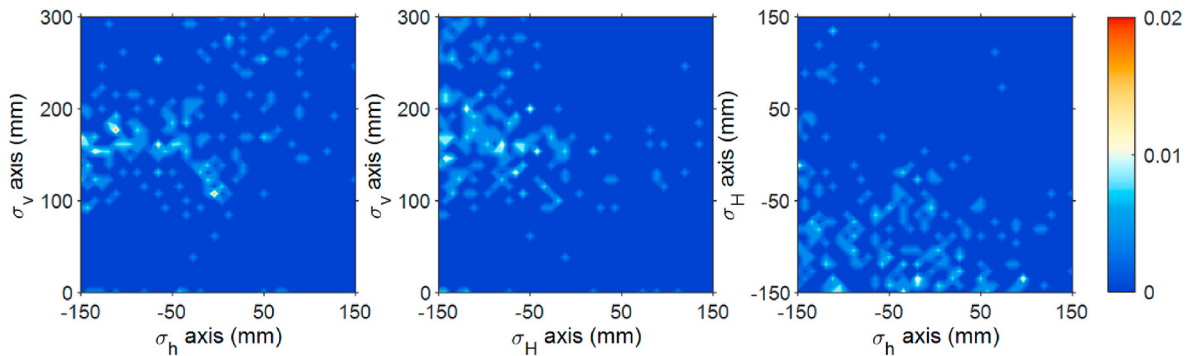


Fig. 5. The dots density of AE event location. The dots density is calculated by the ratio of the number of AE events in the local area, and here a cube of 40 mm³ is used to count the number of AE events. The results are projected in three views, $\sigma_h - \sigma_v$, $\sigma_H - \sigma_v$ and $\sigma_h - \sigma_H$, respectively.

et al.⁴⁴ used box dimensions to illustrate the spatial complexity of the fracture network and show that the fractal dimension increases during the failure process of rock. The fractal method can help obtain a quantitative description of the characteristic of three-dimensional fractures. To describe such fracture morphology in SC-CO₂ fracturing, we use the box-counting method to calculate the fractal dimension.⁴⁴ The higher the fractal value is, the more complicated the fracture network is. The formula of box-counting for fractal dimension is

$$D = \lim_{r \rightarrow 0} \frac{\log_{10} N(r)}{\log_{10}(r)} \quad (3)$$

where the sample space of rock is divided into small box spaces with length r , and $N(r)$ is the number of boxes containing AE event location dots. The length r of the box starts from 1 mm to the maximum value of 300 mm. Each value of r corresponds to an $N(r)$. Then, we plot the results in a logarithmic scale to obtain the fractal dimension D , as is the slope of $\log_{10}(r) - \log_{10}(N(r))$ curve in the linear area (Fig. 6). The calculated D value of our SC-CO₂ generated fractures is 1.56.

3.3. Moment tensor analysis and mechanism of fractures

The AE mechanism can reflect the mechanism of generated fractures. The commonly used methods for solving the AE mechanism are polarity statistics and moment tensor inversion,⁴⁵ and both can classify fractures according to tension-shear property. The moment tensor method can classify and calculate the orientation of fractures.⁴⁶ The moment tensor

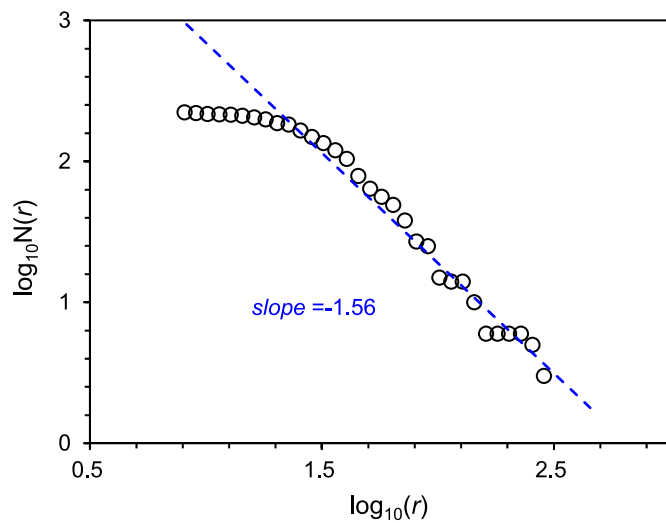


Fig. 6. The result of box-counting fractal dimension. Because of the limitation of AE event positioning accuracy, the smaller-scale area is ignored, i.e., only the linear part with larger-scale is considered for fractal dimension fitting.

of an AE can be inverted by the polarity statistics and amplitude of the P -wave. Ohtsu⁴⁷ first applied this method based on the simplified green function. The components of a moment tensor contain the properties of a fracture. By decomposing the moment tensor (Fig. 7), the fracture properties can be divided into three types, i.e., the tensile, shear, and mixed, which form the mechanical foundation of fracture propagation. However, the propagation of fractures is a process that changes with time, and it is hard to understand the process only by the properties of fractures. We define a mechanism index (MI) for the shear-type AE as 1, tensile-type AE as -1 , and mixed-type AE as 0 (Table 1). The MI is added over time to obtain the accumulated MI. If a shear-type AE appears, the accumulated MI is added by 1, and an increasing trend can be observed on the accumulated MI curve (see Fig. 8). On the contrary, if a tensile-type AE arises, the accumulated MI is subtracted by -1 , and the accumulated MI curve will display a descending trend. The mix-type AE has the value of 0 and will not change on the accumulated MI curve. Therefore, when the curve shows an increasing trend, the propagation of fractures is dominated by shear-type; when the curve presents a decreasing trend, the propagation of fractures is dominated by tensile type. SC-CO₂ fracturing shows an increasing trend in the initiation stage. While in the propagation stage, the curve has apparent downward fluctuations (Fig. 8). This demonstrates that it is easy to generate shear fractures in the initiation stage, while in the propagation stage, tensile fractures are dominant.

3.4. Frequency spectrums of AE waveforms

The AE acquisition system records the entire waveform during the fracturing process. The waveform frequency is determined by the AE source and affected by the AE wave's spreading path. The main influencing factors on the spreading path are the attenuation of wave energy

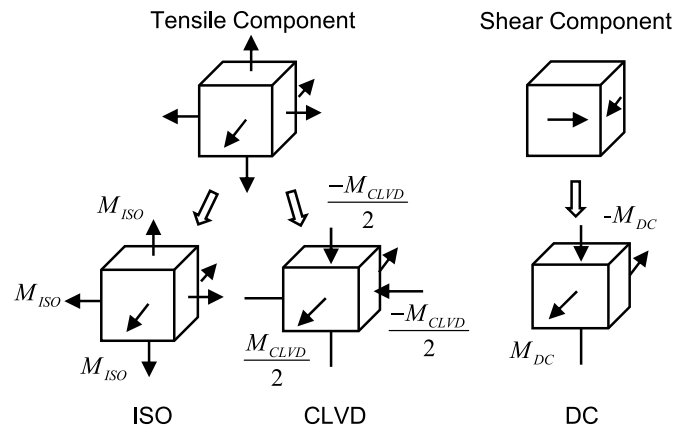


Fig. 7. Decomposition of moment tensor (modified from Ohtsu⁴⁷).

Table 1
Definition of mechanism index.

Range of shear component	Fracture Type	Mechanism Index (MI)
DC > 60%	Shear type	1
DC < 40%	Tensile type	-1
40% ≤ DC ≤ 60%	Mix type	0

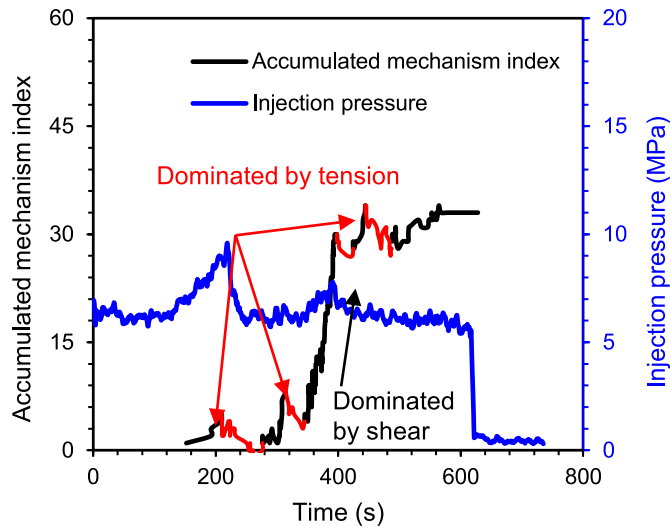


Fig. 8. Accumulated mechanism index over time (black & red line) and injection pressure (blue line) over time. The descending curve segment represents that the tensile-type fractures are dominant (red); the increasing curve segment means that the shear-type fractures are dominant (black). (For interpretation of the references to colour in this figure legend, the reader is referred to the Web version of this article.)

and the limitation of sensors' frequency band. The uncertain influence of these factors leads to the difficulty of analyzing the waveform in the frequency domain. For this reason, we study the frequency of the AE waveform in the SC-CO₂ fracturing process by comparing it with the AE waveform in water fracturing obtained from the same recording system and the same type of rock. By doing so, we limit the influence of rock samples and AE sensors. The waveform of water fracturing is shown in

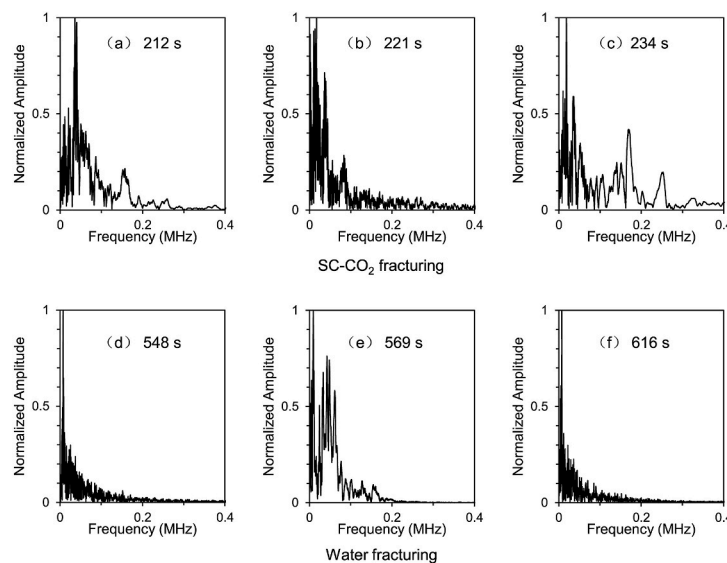


Fig. 9. Top row: (a–c) the frequency spectrums of three typical AE events in SC-CO₂ fracturing. Bottom row: (d–f) the frequency spectrums of three typical AE events in water fracturing.

Fig. 2b. We select three typical AE events with high amplitude, corresponding to 548 s, 569 s, and 616 s, respectively, in the fracturing propagation stage of the water fracturing experiment. Because there are many AE events with high amplitude in the SC-CO₂ experiment (Fig. 2a), we evenly chose three events at the time 212 s, 221 s, and 234 s. The waveform spectrums obtained by fast Fourier transformation for SC-CO₂ fracturing and water fracturing experiments are shown in Fig. 9. The maximum amplitude normalizes the amplitudes in the spectrogram to facilitate comparison. In the spectrogram of AE waveform in SC-CO₂ fracturing (top row of Fig. 9), there are relatively more components (especially in Fig. 9a and b) with a frequency higher than 0.1 MHz, compared to the spectrogram of AE waveform in water fracturing (bottom row of Fig. 9). The major frequency component of the spectrogram for AE events at 548 s and 616 s in water fracturing is less than 0.05 MHz (Fig. 9d–f). We also calculate the time-frequency diagram using wavelet transformation (Fig. 10). The results confirm that the AE events in SC-CO₂ fracturing contain more high-frequency components, i. e., the time-frequency diagram of SC-CO₂ fracturing (left column of Fig. 10) contains more areas with high-frequency values than those in the water fracturing diagram (right column of Fig. 10).

4. Discussions

We have obtained the amplitude, spatial distribution, focal mechanism, and waveform frequency of AE events during SC-CO₂ fracturing from the experimental AE monitoring data. Next, we will discuss the characteristics of fractures formed by SC-CO₂ fracturing from the aspects of fracture morphology and the mechanical mechanism by comparing them with the water fracturing experiments.

4.1. Spatial characteristics of fracture network

The location of AE events and their fractal dimension can reflect the features of the generated fracture network morphology. We compare the fracture network caused by SC-CO₂ fracturing with that by water fracturing published in Wu et al.²⁷ We chose two rock samples for water fracturing experiments, and they are labeled as LMX1 and LMX2. The rock samples after the fracturing experiment are shown in Fig. 11a–b. According to the AE event location (Fig. 11c–d), more generated fractures cover a larger rock volume in LMX1. While in LMX2, the induced fractures are more concentrated near the injecting point and only cover a small rock volume due to the constrain of bedding. The difference in

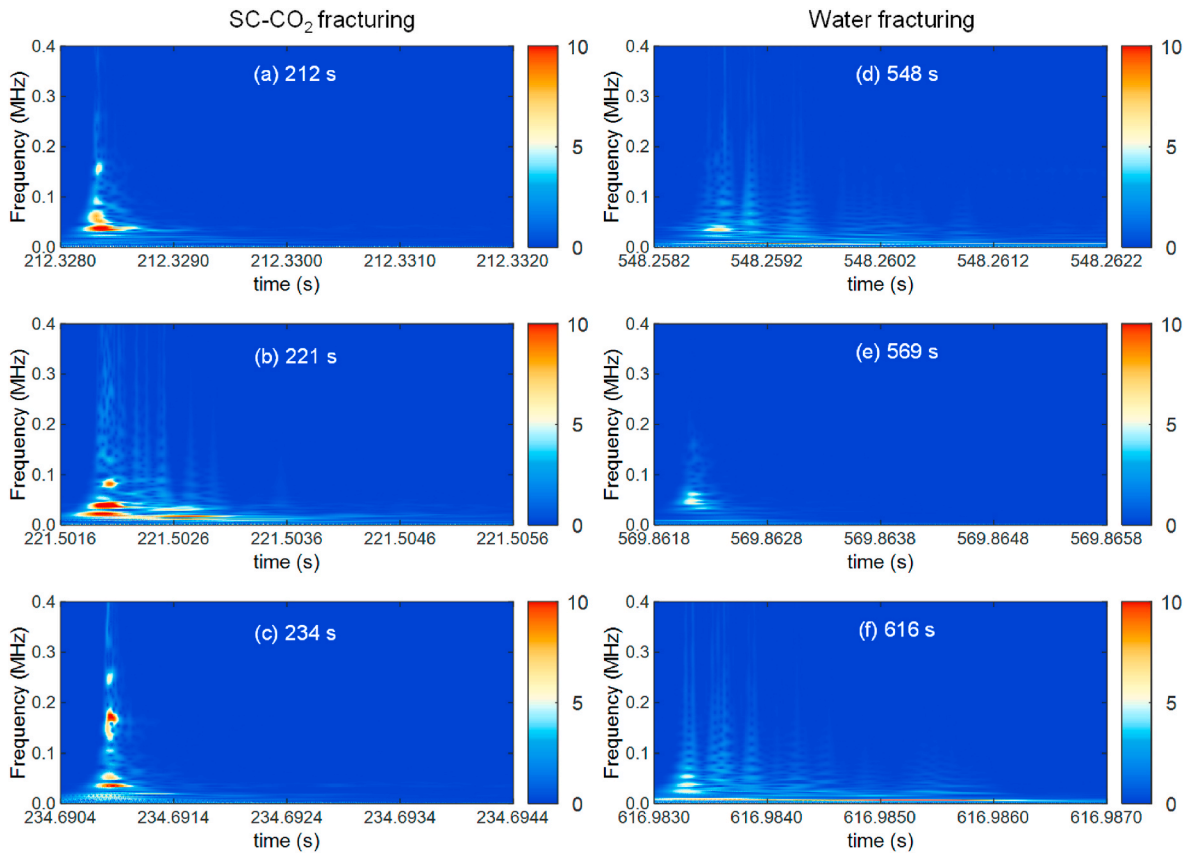


Fig. 10. The time-frequency diagram of AE events with high amplitude in the fracturing propagation stage in (a–c) SC-CO₂ (left column) and (d–f) water fracturing (right column) experiments.

the stimulated rock volume between LMX1 and LMX2 is caused by the different water permeability at the bedding area. And, this permeability difference is induced by the different vertical stress. The stimulated volume in LMX2 is similar to that in the SC-CO₂ fracturing. The reason for such a small stimulated volume in both LMX2 in water fracturing and the previous SC-CO₂ fracturing may lie in the bedding structures in rock samples. The high permeability of the bedding structures leads to an increased release of energy carried by the fracturing fluid. In addition, the low viscosity of SC-CO₂ makes it easier to be filtered through the bedding structures. Therefore, shale bedding is a critical factor affecting the stimulated volume of the SC-CO₂ fracturing. We plot the density map of the AE event location for the two samples for water fracturing (Fig. 11). The figures show a more concentrated area of AE events near the injecting point, which is different from the results in SC-CO₂ fracturing (Fig. 5). The fluid energy carried by SC-CO₂ is more widely distributed than that of water due to the high permeability of SC-CO₂ in rock. The fractal dimension of the generated fractures in SC-CO₂ fracturing ($D = 1.56$) is close to that in LMX2 in water fracturing ($D = 1.50$). However, both are lower than that in LMX1 in water fracturing ($D = 1.79$). The ultimate goal of hydraulic fracturing is to generate large and complex fracture networks. It seems easier to achieve this goal with SC-CO₂ as it can release energy more evenly. However, due to the constrain from the bedding structure, the complexity of the generated fracture network in SC-CO₂ fracturing is not as high as that predicted by the theory.

4.2. Mechanism of the fracturing process

The mechanism index curve of SC-CO₂ fracturing shows an increasing trend in the initiation stage, which means the shear fractures dominate the failure process. We calculate the percentages of different

fracture types in the initiation stage and compare them with those in water fracturing (LMX1 as an example) in Fig. 12. The results demonstrate that more shear fractures are generated in SC-CO₂ fracturing. In the traditional tensile failure model, the fracture propagates along the direction of maximum principal stress. However, the initiation stage may be complicated for reservoirs with developed bedding. Li et al.²⁰ show an extensive fluctuation range of initiation pressure due to the influence of bedding. Two possibilities could lead to a complicated initiation stage. One is the heterogeneity of rock strength at the wellhead caused by bedding, and the other is the heterogeneity of stress distribution caused by the interaction of fluid and bedding. The former comes from the influence of rock properties, and the latter is influenced by fluid-solid coupling. The results of Zhou et al.⁴⁸ and Zou et al.²² also show that the initiation pressure reduced obviously in the same rock but with SC-CO₂, which indicates that the impact of fluid-solid coupling is more significant. For our experiment, the initiation pressure is 9.6 MPa. But the classical formula for evaluating the initiation pressure based on the tensile failure model is

$$P_{ini} = (3\sigma_h - \sigma_H) - \sigma_t \quad (4)$$

where σ_t is the tensile strength of rock. The tensile strength of the current shale specimen is near 15 MPa. According to Eq. (4), the initiation pressure is approximately 30 MPa under the triaxial stress condition of $\sigma_h = 10$ MPa, $\sigma_H = 15$ MPa, and $\sigma_v = 20$ MPa. This is higher than our results. The reason may be that the SC-CO₂ can easily invade the bedding structure or the natural fractures around the wellhead and change the local stress condition (Fig. 13). Therefore, more shear-tensile mixed failure and pure shear failure appear at the wellhead. The traditional model for the initiation pressure cannot cover the hybrid failure process, which results in an inaccurate prediction.

The properties of the generated fractures in the propagation stage

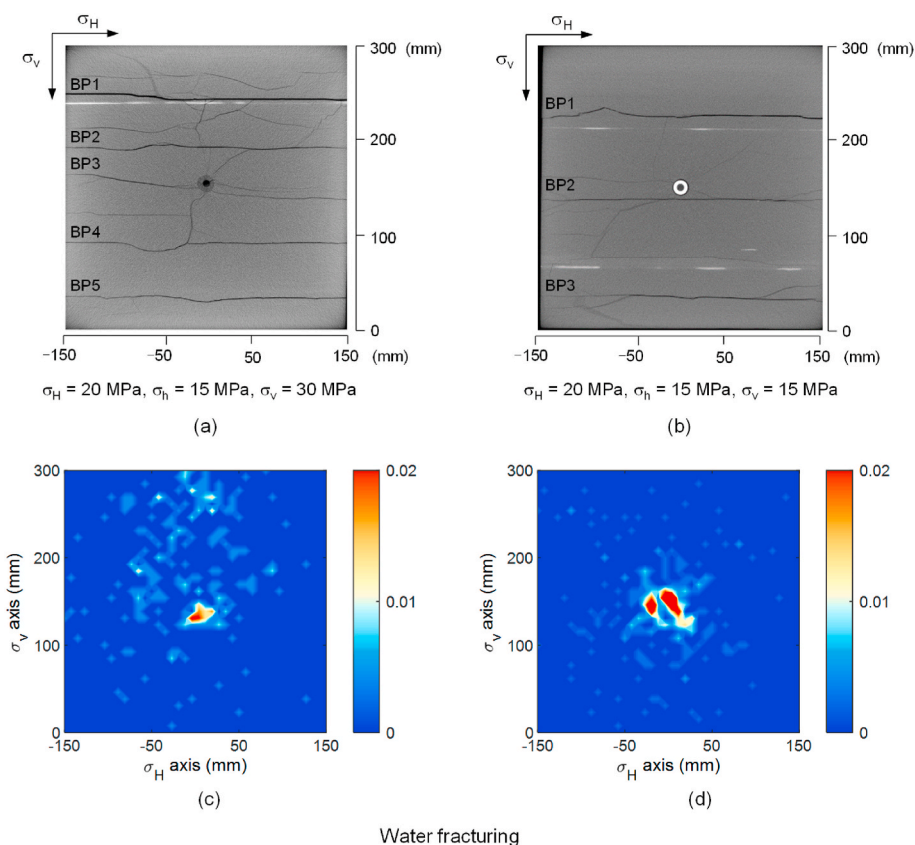


Fig. 11. (a) CT scanning slice of water fracturing rock sample (LMX1). The scanning plane is parallel to the $(\sigma_H - \sigma_v)$ view at around -20 mm distance of the σ_h direction. The bedding planes are labeled in a CT scanning slice of the rock sample (modified from Wu et al.²⁷) (b) CT scanning slice of water fracturing (LMX2). It has nearly the same scanning position as LMX1. (c) The dots density map of AE event locations of LMX1 at $(\sigma_H - \sigma_v)$ view (all points are projected on the $(\sigma_h - \sigma_H)$ view). (d) The dots density map of AE event locations of LMX1 at $(\sigma_H - \sigma_v)$ view.

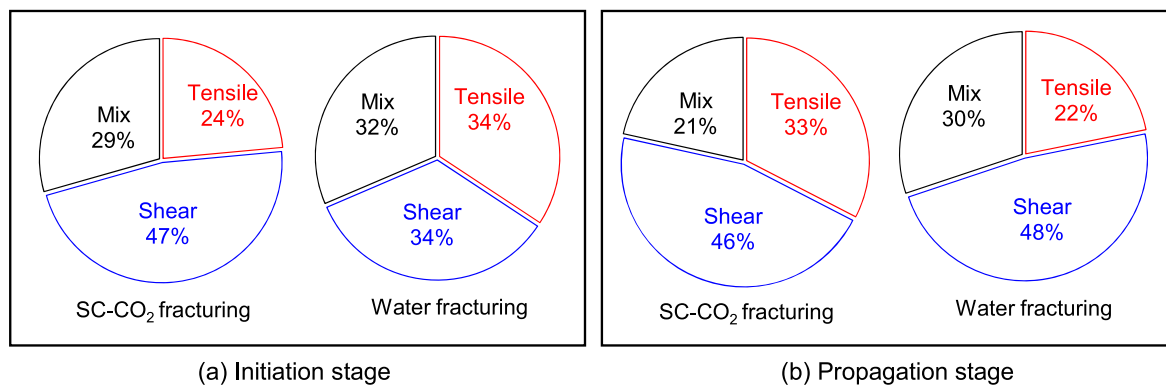


Fig. 12. The statistics of hydraulic fracturing mechanism.

show a different result. More tensile fractures are caused in the propagation stage in SC-CO₂ fracturing (Fig. 12b). This phenomenon can be explained by the effect of fluid lag in fracture tips. In the process of fracture propagation, the fluid front usually lags behind the fracture front. The lag region increases the fracture toughness at the tip (Fig. 14). Jeffrey⁴⁹ proposes a fracture toughness of lag and re-defines the tip's fracture toughness as the effective toughness. The larger the fluid lag region is, the higher the effective toughness. SC-CO₂ could easily enter the fracture tips due to its strong permeability, resulting in a small lag region and thus a low effective fracture toughness. Since fracture toughness has a significant influence on hydraulic fracture propagation under toughness regime and the fracturing process in laboratory scale is usually toughness-controlled, the more vital permeability of SC-CO₂ at fracture tips can explain the more significant number of generated tensile fractures in the propagation stage. Previous results indicated that

low viscosity might induce shear-dominant fractures, whereas high viscosity fluid tends to induce tensile-dominant fractures.¹⁹ Our results are not contrary to this because we only claim more tensile fractures in the propagation stage. Additionally, the size of our sample ($300 \times 300 \times 300$ mm³) is larger than the sample size ($170 \times 170 \times 170$ mm³) in the experiment of Ishida et al.,¹⁹ which leads to a large area for the propagation of fractures, thus inducing more tensile fractures.

It should be noted, in our results, there are more shear-type fractures than tensile in both water and SC-CO₂ fracturing. This may be caused by the sensitivity of the AE sensor (RS-2A) to shear fractures. This type of AE sensor has a relatively low-frequency band (50–400 kHz) than the sensors applied in other experiments,¹⁹ such as the sensor with a resonance frequency of 300 kHz and a band-pass filter between 80 kHz and 1 MHz. The shear-type fractures usually contain more low-frequency components.⁵⁰ In addition, the criteria for classifying the shear-type

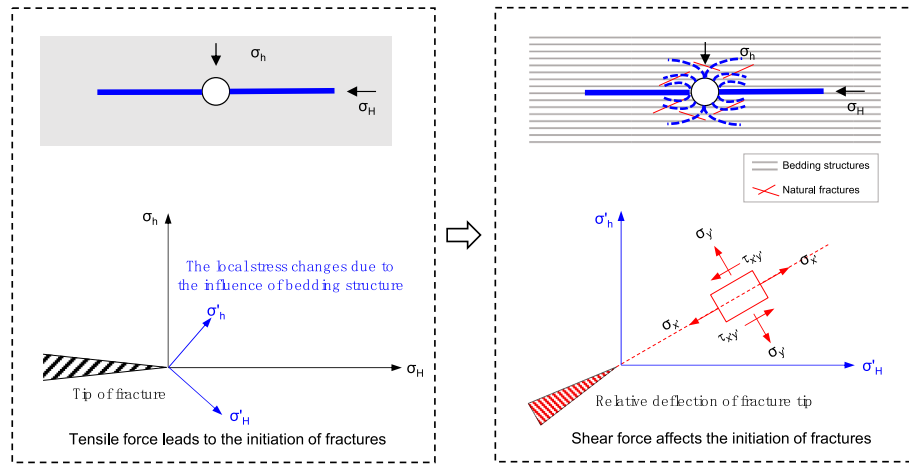


Fig. 13. Schematic diagram of bedding activation by hydraulic fractures at the injection point. If there is no bedding structure, the hydraulic fractures will propagate in the σ_H -axis direction (left column). If the bedding structures exist, the local stress would change, as it shows that the local stress coordinate system would rotate relative to the tip of fractures (right column). In the new stress coordinate, a shear force component will be generated.

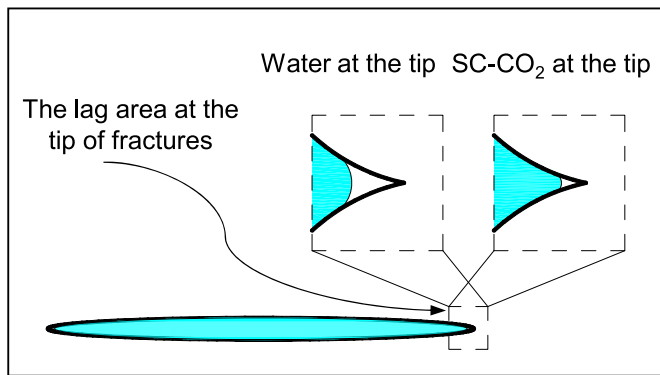


Fig. 14. Schematic diagram of fracture lag.

AE by the moment tensor may also lead to the preferred shear-type fractures in shale. The reason is that shales are often anisotropic, which affects the inversion and decomposition of moment tensor. Future works should be conducted to investigate new criteria for classifying the shear-tensile fractures in shale. Nevertheless, our conclusions that the more tensile fractures in the propagation stage and more shear-type fractures in the initiation stage of SC-CO₂ fracturing can be observed are based on the comparison with water fracturing in the same type of shale rock. The errors induced by sensor sensitivity and the inversion of moment tensor are negligible.

The AE rate is closely related to the fracture propagation speed. The active period of AE rates represents successive fractures. In water fracturing, there is an intense outbreak of AE events near the peak of injection pressure. After this, in the propagation stage, the AE event tends to be quiet (Fig. 2a). However, in SC-CO₂ fracturing, the AE events stay active for a long period (Fig. 2b), which indicates an unstable propagation of fractures in SC-CO₂ fracturing. In addition, in the propagation stage, the amplitudes of AE events in SC-CO₂ fracturing are generally higher than those in water fracturing. For comparison, we further calculate the *b*-values of water fracturing experiments in Li et al.²⁰ The *b*-values in water fracturing are generally between 1.2 and 1.8; however, the *b*-value in the current SC-CO₂ fracturing is 0.94. This demonstrates that the SC-CO₂ fracturing could generate more AE events with large amplitude, and implies that fractures are easier to form in SC-CO₂ fracturing. In sum, the results above (i.e., continuously high AE rate and lower *b*-value) show that fractures propagate faster and energy transfers more efficiently in SC-CO₂ fracturing.

4.3. Phase change of CO₂ and the high-frequency AE events

There are two possible phase changes of SC-CO₂. One is from the supercritical state to the gaseous state, and the other is from the supercritical state to liquid. According to the phase change diagram of CO₂ shown in Fig. 15, the former is controlled by temperature, while the latter is controlled by pressure. In our experiment, the temperature change is mainly due to the temperature evaluation of rock material, which is either constant or changes within a low-frequency change. Therefore, the speed of the phase changes caused by temperature should be synchronized with or even lower than the speed of fracture propagation. However, the phase changes caused by pressure may couple in the process of fracture propagation. The fracture volume increased when the fracture expanded, leading to a pressure decrease inside the fracture. Then SC-CO₂ becomes gaseous according to the phase change diagram. The increasing importance of gaseous CO₂ will generate an impact pressure on the fracture tip and thus accelerate the propagation of fractures.

There is a high-frequency region in the AE waveform of SC-CO₂ compared with water fracturing (Fig. 10). The high frequency is over 0.15 MHz and indicates a high speed of energy release. Such a rapid energy release may come from a high propagation speed of the fractures. Therefore, the change of frequency of this process is higher than that of water fracturing. The observation of higher frequency AE events supports CO₂ phase change from the supercritical state to a gaseous state.

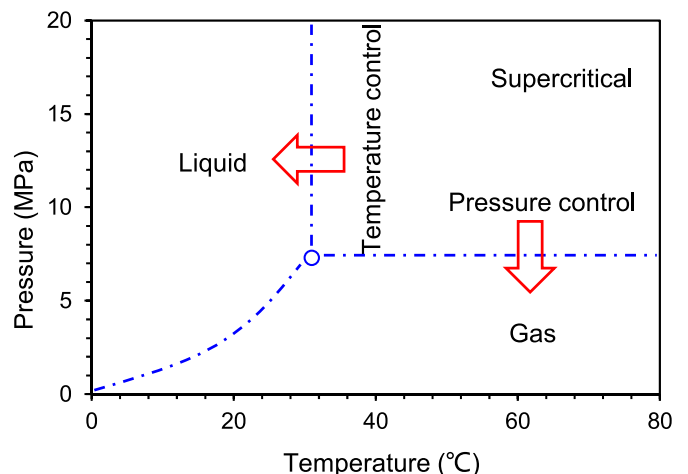


Fig. 15. Phase change diagram of CO₂ (modified from Zhou & Zhang²³).

SC-CO₂ can generate irregular fracture morphology, which has been proved by the dispersed distribution of AE event location (Fig. 5). In addition to the influence of permeability mentioned above, the phase change of CO₂ during the fracturing process could also contribute to the irregular fracture morphology. Because the process of phase changes is similar to stress shock at the fracture tip, it will lead to a fracture branching and result in local complexity of fractures.

5. Conclusions

We have investigated the characteristics of SC-CO₂ fracturing in shale reservoir rocks using AE monitoring. Combined with the unique physical and chemical properties of CO₂, we have analyzed the spatial distribution of AE events, generated fracture morphology, investigated the mechanical mechanism of fracture network formed under SC-CO₂ fracturing. For LMX shale, due to the effect of bedding, the fracturing process has a small expansion area, and the AE event locations are scattered. In addition, the fractal index of AE points is lower than the fracture network in water fracturing. According to the moment tensor analysis of AE events, more shear fractures are formed in the initiation stage under SC-CO₂ fracturing. This is because the SC-CO₂ activates the natural fractures near the head of the well and complicates the fracturing process. Because of its high permeability, SC-CO₂ can easily reach the tip of fractures during the propagation process, which reduces the lag of fluid inside the fractures, energizes the fracture, and guarantees the propagation induced by tensorial stress. Therefore, SC-CO₂ promotes the generation of fractures and limits the energy loss from the fracture. However, it is more vulnerable to bedding. SC-CO₂ could constantly generate AE events with high amplitude and high frequency compared to water fracturing. There are more high-frequency AE components in SC-CO₂ fracturing than those in water fracturing. The high-frequency components are closely related to the phase change of CO₂, which is a special effect of SC-CO₂ fracturing.

To conclude, in the process of SC-CO₂ fracturing, bedding structures and phase change of CO₂ have strong influences not only on the initiation of fractures but also the propagation. All the factors lead to the unique characteristic of SC-CO₂ fracturing, which shows a pretty different fracture morphology and mechanical mechanism than water fracturing. Our study could provide a further understanding of the application of SC-CO₂ as a fracturing fluid in the development of shale oil and gas reservoirs.

Declaration of competing interest

The authors declare that they have no known competing financial interests or personal relationships that could have appeared to influence the work reported in this paper.

Acknowledgment

The authors express thanks for financial support from the subprojects of the Strategic Cooperation Technology Projects of CNPC and CUPB (ZLZX2020-01-08 and ZLZX2020-01-07), and the Natural Science Foundation of China (No. 51774236).

References

- 1 Warpinski NR, Mayerhofer MJ, Vincent MC, Cipolla CL, Lonon EP. Stimulating unconventional reservoirs: maximizing network growth while optimizing fracture conductivity. *J Can Pet Technol*. 2009;48:39–51.
- 2 Vermilyen J, Zoback MD. Hydraulic fracturing, microseismic magnitudes, and stress evolution in the Barnett Shale, Texas, USA. In: *SPE Hydraulic Fracturing Technology Conference*. Society of Petroleum Engineers; 2011.
- 3 King GE. Thirty years of gas shale fracturing: what have we learned?. In: *SPE Annual Technical Conference and Exhibition*. Society of Petroleum Engineers; 2010.
- 4 Ge H, Yang L, Yinghao Shen, et al. Experimental investigation of shale imbibition capacity and the factors influencing loss of hydraulic fracturing fluids. *Petrol Sci*. 2015;12:636–650.
- 5 Xing Huang, Lijun Gu, Shuaishuai Li, Yifan Du, Yueliang Liu. Absolute adsorption of light hydrocarbons on organic-rich shale: An efficient determination method. *Fuel*. 2021;121998.
- 6 Heller R, Zoback M. Adsorption of methane and carbon dioxide on gas shale and pure mineral samples. *J Unconv. Oil Gas Resour*. 2014;8:14–24.
- 7 Wang H, Li G, Shen Z. A feasibility analysis on shale gas exploitation with supercritical carbon dioxide. *Energy Sources, Part A Recovery, Util Environ Eff*. 2012; 34:1426–1435.
- 8 Ishida T, Desaki S, Yamashita H, et al. Injection of supercritical carbon dioxide into granitic rock and its acoustic emission monitoring. *Procedia Eng*. 2017;191:476–482.
- 9 Li S, Zhang S, Zou Y, et al. Experimental study on the feasibility of supercritical CO₂-gel fracturing for stimulating shale oil reservoirs. *Eng Fract Mech*. 2020;238, 107276–107276.
- 10 Middleton R, Viswanathan H, Currier R, Gupta R. CO₂ as a fracturing fluid: potential for commercial-scale shale gas production and CO₂ sequestration. *Energy Proc*. 2014; 63:7780–7784.
- 11 Zhao Z, Li X, He J, Mao T, Zheng B, Li G. A laboratory investigation of fracture propagation induced by supercritical carbon dioxide fracturing in continental shale with interbeds. *J Petrol Sci Eng*. 2018;166:739–746.
- 12 Cai C, Kang Y, Yang Y, et al. The effect of shale bedding on supercritical CO₂ jet fracturing: a experimental study. *J Petrol Sci Eng*. 2020;195:107798.
- 13 Edlmann K, Haszeldine S, McDermott CI. Experimental investigation into the sealing capability of naturally fractured shale caprocks to supercritical carbon dioxide flow. *Environ Earth Sci*. 2013;70:3393–3409.
- 14 Xing Huang, Yu Zhang, Mengqing He, Xiang Li, Weipeng Yang, Jun Lu. Asphaltene precipitation and reservoir damage characteristics of CO₂ flooding in different microscopic structure types in tight light oil reservoirs. *Fuel*. 2022;122943.
- 15 Hou B, Chen M, Tan P, Li D. Monitoring of hydraulic fracture network by acoustic emission method in simulated tri-axial fracturing system of shale gas reservoirs. *J China Univ Pet*. 2015;39:66–71.
- 16 Lei X, Ma S. Laboratory acoustic emission study for earthquake generation process. *Earth Sci*. 2014;27:627–646.
- 17 Petružálek M, Jechumtálová Z, Kolář P, et al. Acoustic emission in a laboratory: mechanism of microearthquakes using alternative source models. *J Geophys Res Solid Earth*. 2018;123:1–18.
- 18 Hampton JC, Matzar L, Hu D, Gutierrez M. *Fracture Dimension Investigation of Laboratory Hydraulic Fracture Interaction with Natural Discontinuity Using Acoustic Emission*. San Francisco, California: American Rock Mechanics Association; 2015, 7–7.
- 19 Ishida T, Chen Y, Bennour Z, et al. Features of CO₂ fracturing deduced from acoustic emission and microscopy in laboratory experiments. *J Geophys Res Solid Earth*. 2016; 121:8080–8098.
- 20 Li N, Zhang S, Zou Y, et al. Acoustic emission response of laboratory hydraulic fracturing in layered shale. *Rock Mech Rock Eng*. 2018;51:3395–3406.
- 21 Zhang X, Lu Y, Tang J, Zhou Z, Liao Y. Experimental study on fracture initiation and propagation in shale using supercritical carbon dioxide fracturing. *Fuel*. 2017;190: 370–378.
- 22 Zou Y, Li N, Ma X, Zhang S, Li S. Experimental study on the growth behavior of supercritical CO₂ induced fractures in a layered tight sandstone formation. *J Nat Gas Sci Eng*. 2018;49:145–156.
- 23 Zhou D, Zhang G. A review of mechanisms of induced fractures in SC-CO₂ fracturing. *Petroleum Science Bulletin*. 2020;2:239–253.
- 24 Ono K. Calibration methods of acoustic emission sensors. *Materials*. 2016;9, 508–508.
- 25 Grosse CU, Ohtsu M. *Acoustic Emission Testing*. Springer Science & Business Media; 2008.
- 26 Zou Y, Ma X, Zhou T, et al. Hydraulic fracture growth in a layered formation based on fracturing experiments and discrete element modeling. *Rock Mech Rock Eng*. 2017; 50:2381–2395.
- 27 Wu S, Li T, Ge H, Wang X, Li N, Zou Y. Shear-tensile fractures in hydraulic fracturing network of layered shale. *J Petrol Sci Eng*. 2019:183.
- 28 Li N, Zhang S, Zou Y, Ma X, Wu S, Zhang Y. Experimental analysis of hydraulic fracture growth and acoustic emission response in a layered formation. *Rock Mech Rock Eng*. 2018;51:1047–1062.
- 29 Ishida T, Aoyagi K, Niwa T, et al. Acoustic emission monitoring of hydraulic fracturing laboratory experiment with supercritical and liquid CO₂. *Geophys Res Lett*. 2012;39.
- 30 Hampton JC. *Laboratory Hydraulic Fracture Characterization Using Acoustic Emission*. Colorado School of Mines; 2012.
- 31 Wang D, Ge H, Wang X, et al. A novel experimental approach for fracability evaluation in tight-gas reservoirs. *J Nat Gas Sci Eng*. 2015;23:239–249.
- 32 Wu S, Ge H, Wang X, Meng F. Shale failure processes and spatial distribution of fractures obtained by AE monitoring. *J Nat Gas Sci Eng*. 2017;41:82–92.
- 33 Colombo IS, Main IG, Forde MC. Assessing damage of reinforced concrete beam using “b-value” analysis of acoustic emission signals. *J Mater Civ Eng*. 2003;15:280–286.
- 34 Meng F, Ge H, Yan W, Wang X, Wu S, Wang J. Effect of saturated fluid on the failure mode of brittle gas shale. *J Nat Gas Sci Eng*. 2016;35:624–636.
- 35 Schumacher T, Straub D, Higgins C. Toward a probabilistic acoustic emission source location algorithm: a Bayesian approach. *J Sound Vib*. 2012;331:4233–4245.
- 36 Ge M, Kaiser PK. Interpretation of physical status of arrival picks for microseismic source location. *Bull Seismol Soc Am*. 1990;80:1643–1660.
- 37 Waldhauser F, Ellsworth WL. A double-difference earthquake location algorithm: method and application to the northern Hayward fault, California. *Bull Seismol Soc Am*. 2000;90:1353–1368.
- 38 Sedlak P, Hirose Y, Enoki M. Acoustic emission localization in thin multi-layer plates using first-arrival determination. *Mech Syst Signal Process*. 2013;36:636–649.

- 39 Zhang J, Tang Y, Li H. STA/LTA fractal dimension algorithm of detecting the P-wave arrival. *Bull Seismol Soc Am*. 2017;108:230–237.
- 40 Dontsov EV, Peirce AP. An enhanced pseudo-3D model for hydraulic fracturing accounting for viscous height growth, non-local elasticity, and lateral toughness. *Eng Fract Mech*. 2015;142:116–139.
- 41 Peirce A. Modeling multi-scale processes in hydraulic fracture propagation using the implicit level set algorithm. *Comput Methods Appl Mech Eng*. 2015;283:881–908.
- 42 Guo T, Zhang S, Ge H, Wang X, Lei X, Xiao B. A new method for evaluation of fracture network formation capacity of rock. *Fuel*. 2015;140:778–787.
- 43 Lei X. Evolution of b-value and fractal dimension of acoustic emission events during shear rupture of an immature fault in granite. *Appl Sci*. 2019;9, 2498–2498.
- 44 Li Y, Liu J, Zhao X, Yang Y. Study on b-value and fractal dimension of acoustic emission during rock failure process. *Rock Soil Mech*. 2009;30:2559–2563.
- 45 Graham CC, Stanchits S, Main IG, Dresen G. Comparison of polarity and moment tensor inversion methods for source analysis of acoustic emission data. *Int J Rock Mech Min Sci*. 2010;47:161–169.
- 46 Manthei G, Eisenblätter J, Dahm T. Moment tensor evaluation of acoustic emission sources in salt rock. *Construct Build Mater*. 2001;15:297–309.
- 47 Ohtsu M. Simplified moment tensor analysis and unified decomposition of acoustic emission source: application to in situ hydrofracturing test. *J Geophys Res Solid Earth*. 1991;96:6211–6221.
- 48 Zhou D, Zhang G, Wang Y, Xing Y. Experimental investigation on fracture propagation modes in supercritical carbon dioxide fracturing using acoustic emission monitoring. *Int J Rock Mech Min Sci*. 2018;110:111–119.
- 49 Jeffrey R. The combined effect of fluid lag and fracture toughness on hydraulic fracture propagation. In: *Low Permeability Reservoirs Symposium*. Society of Petroleum Engineers; 1989.
- 50 Zhang Z, Deng J, Zhu J, Li L. An experimental investigation of the failure mechanisms of jointed and intact marble under compression based on quantitative analysis of acoustic emission waveforms. *Rock Mech Rock Eng*. 2018;51:2299–2307.